Dynamic Wheel-Soil Model for Lightweight Mobile Robots with Smooth Wheels

Rishad A. Irani, Robert J. Bauer & Andrew Warkentin

Journal of Intelligent & Robotic Systems
with a special section on Unmanned Systems

ISSN 0921-0296

J Intell Robot Syst
DOI 10.1007/s10846-012-9777-3

Springer

J Intell Robot Syst
DOI 10.1007/s10846-012-9777-3

Dynamic Wheel-Soil Model for Lightweight Mobile Robots with Smooth Wheels

Rishad A. Irani · Robert J. Bauer · Andrew Warkentin

Received: 3 October 2011 / Accepted: 16 August 2012

Abstract This paper extends traditional wheel–soil modeling for lightweight mobile robots operating with smooth wheels on dry sandy soil to capture the transient oscillations that have been observed in drawbar pull measurements. To model these drawbar pull fluctuations, a new dynamic pressure–sinkage relationship was extrapolated from the literature and experimental observations of smooth rigid wheels operating in sandy soil. The resulting two-dimensional high-fidelity analytical model was validated with a unique single-wheel testbed designed from a Blohm Planomat 408 computer-numerically-controlled creep-feed grinding machine. For the experimental conditions used in this research, the resulting model is able to predict the fluctuating values of the drawbar pull for a variety of slip ratios and normal loads tested with a smooth rigid wheel in sandy soil. The new model was tuned at a single normal load over a variety of slip ratios and was then able to predict the amplitude and frequency of the oscillations about the mean drawbar pull at different normal loads and slip ratios.

Keywords Wheel-soil modeling · Rigid wheel · Mobile robots · Planetary rovers · Terrain interaction

R. A. Irani (✉) · R. J. Bauer · A. Warkentin
Department of Mechanical Engineering,
Dalhousie University, Halifax, NS, Canada
e-mail: rirani@dal.ca

R. J. Bauer
e-mail: robert.bauer@dal.ca

A. Warkentin
e-mail: andrew.warkentin@dal.ca

1 Introduction

Research examining vehicle-terrain interaction expanded significantly during the 1940's due to World War II. During this period, myriad researchers examined how tracked and wheeled vehicles interacted with the ground to assess the feasibility of proceeding over a specified terrain. The U.S. Army Corps of Engineers developed a 'Go' and 'No-Go' methodology to determine if a single vehicle or convoy could pass over a given terrain or path [4]. Today the field has been expanded to incorporate mission planning and design of lightweight mobile robots, such as planetary rovers, to assess suspension, mobility and climbing capabilities.

In the interest of developing high-fidelity models of wheel–soil interactions, a single-wheel testbed (SWTB) is typically used by researchers. For example, Maciejewski and Jarzębowski [17] used

Published online: 04 September 2012

a SWTB housing a rigid rolling cylinder with a diameter of 32cm to examine the influence of slip, number of passes and the friction coefficient on the drawbar pull of the system. The researchers used a mix of cement, bentonite sand and white Vaseline with no added water as their terrain. For the towed smooth cylindrical wheel operating at steady-state slip conditions, it was noticed that the resulting track pattern in the soil had repeatable cracks in it. Both the depth of the crack and the mean distance between cracks appeared to be related to the normal load, which varied from 500 to 4000 N.

Research funded by NASA and carried out by Apostolopoulos et al. [1] used a SWTB to study a large inflatable smooth wheel on analogous Martian surfaces. The inflatable wheel had a mass of 15.2 kg, a radius of 70 cm along the compressed axis, and the contact width was approximately 1 m. Their experiments revealed repeating ridges in the resulting wheel track that were 5 cm wide and 3 cm tall. The present authors also noticed similar repeating ridges in the images of Ishigami's PhD thesis [12]. These repeating ridges were in the track of a smooth rigid wheel operating in a Lunar simulant or Toyoura Sand. Ishigami's work, however, concentrated on wheel slip/skid motion for lunar exploration robots rather than the observed repeating ridges in the wheel track.

The present authors used a SWTB to confirm the presence of these ripple patterns in the track of a smooth wheel operating under steady-state slip conditions in sandy soil. These ridges were coupled with distinct and repeatable oscillations in the force and torque data measured by the SWTB. This previously-unexplored phenomenon associated with a smooth wheel operating in sandy soil was reconfirmed by the present authors using a micro rover operating under steady-state slip conditions—evidence that the repeating ridges are not an artifact of a SWTB but, rather, an unmodelled phenomena which is occurring within the wheel–soil interaction.

To capture the non-oscillating mean forces acting on a wheel, Ishigami et al. [13] refined the traditional Bekker formulation [4] and used the work of other researchers such as Wong [23], Reece [20], Janosi and Hanamoto [14] and Hegedus [7] to validate a three-dimensional model that accounts for lateral forces and slippage. This recently-developed model, however, neither predicts the oscillations in the drawbar pull observed by the present authors during steady-state slip conditions, nor does their model explain why the repeating ridges in the track of a smooth wheel are occurring. Such variable loading is hazardous to driveline components and various vehicle peripherals. Furthermore, variations in drawbar pull may impact the vehicle's mobility capabilities. Thus, advancement in the fidelity of smooth-wheel terrain interaction models needs to be made to fully capture these effects and assist in the design of lightweight mobile robots.

This paper offers a wheel–soil modelling foundation which can be integrated with existing analytical models to capture the underlying oscillations in the measured data and effectively increase the fidelity of these smooth-wheel models. This innovation is achieved by adding terms to the analytical wheel–soil model presented by Ishigami et al. [13]. Previous work by the present authors [11] develops an oscillatory model that accounts for periodic variations observed for a wheel with grousers—where the front face of each grouser blade repeatedly comes into contact with the terrain. This previous research, however, does not fully explain how or why such an oscillatory model could be applied to a rigid smooth wheel. It is critical to understand how a rigid smooth wheel interacts with the terrain because this knowledge provides a fundamental building block for developing future high-fidelity wheel–soil models for more complex wheel configurations (such as flexible wheels with grousers). Moreover, the smooth-wheel model developed in this paper is of importance to real-life applications because if a grouser wheel becomes clogged with terrain, as they often do [2], the dynamic grouser model previously presented by the current authors [11] is no longer valid and the smooth-wheel model presented in this article must be applied to the scenario.

This paper is structured as follows: Section 2 derives the proposed smooth-wheel model, Section 3 discusses the SWTB experimental apparatus used to validate the new model, Section 4 presents experimental results to validate the proposed model, and Section 5 draws some conclusions and makes recommendations for future work.

2 Model Development

There are a variety of approaches to model the wheel–soil interaction including analytical [4, 16, 23] and finite element [5, 15, 19] methods. The model presented in the current work is based on traditional analytical wheel–soil modelling approaches of Bekker [4] and Wong [23].

2.1 Traditional Analytical Model

A traditional wheel–soil model [4, 23] calculates the stresses and forces acting on the wheel by assuming that the pressure p under a wheel is an exponential function of the form:

$$p = kz^n \tag{1}$$

where z is the sinkage, n is the sinkage exponent, and k is an empirical coefficient.

The normal stress distribution under the moving wheel is shown in Fig. 1 and is often represented by the following equation as described by Wong and Reece [24]:

$$\sigma(\theta) = \begin{cases} r^n k(\cos\theta - \cos\theta_f)^n & (\theta_m \le \theta < \theta_f) \\ r^n k\left(\cos\left\{\theta_f - \dfrac{\theta - \theta_r}{\theta_m - \theta_r}(\theta_f - \theta_m)\right\} - \cos\theta_f\right)^n & (\theta_r \le \theta < \theta_m) \end{cases} \tag{2}$$

where θ_f and θ_r are determined by the geometry in Fig. 1 as follows:

$$\theta_f = \cos^{-1}(1 - z/r) \tag{3}$$

$$\theta_r = -\cos^{-1}(1 - \eta z/r) \tag{4}$$

and η is a parameter that is related to the height of the terrain in the track left by the wheel. Ishigami et al. [13] stated that terrain, slip ratio and the surface of the wheel can affect the value of η. Both visual and measured observations were used in the present study to estimate η during experimental testing.

The angle at which the maximum normal stress occurs is known as θ_m and some researchers have approximated θ_m as the midpoint between θ_f and θ_r [21]; however, Reece and Wong [24] proposed the following relationship:

$$\theta_m = (b_0 + b_1 i)\,\theta_f \tag{5}$$

where $b_0 \approx 0.4$ and $0.0 \le b_1 \le 0.3$ and i is the slip ratio of the wheel. The slip ratio i is defined as:

$$i = \frac{\omega_w r - V_x}{\omega_w r} \tag{6}$$

where ω_w is the angular velocity of the wheel, r is the radius of the wheel, and V_x is the translational velocity of the wheel centre.

The shear stress acting along the length of the wheel–soil interface is calculated by Janosi and Hanamoto's equation [14]:

$$\tau(\theta) = (c + \sigma(\theta)\tan\phi)\left[1 - e^{-j(\theta)/K}\right] \tag{7}$$

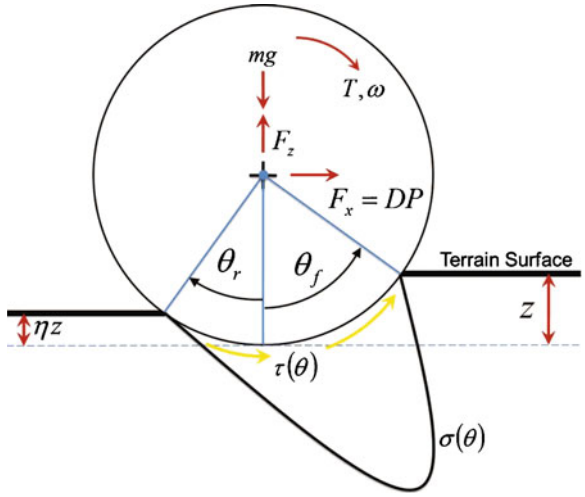

Fig. 1 Stress and Forces acting on the wheel. Note: θ_r is measured from the vertical axis and has a negative numerical value in the configuration shown

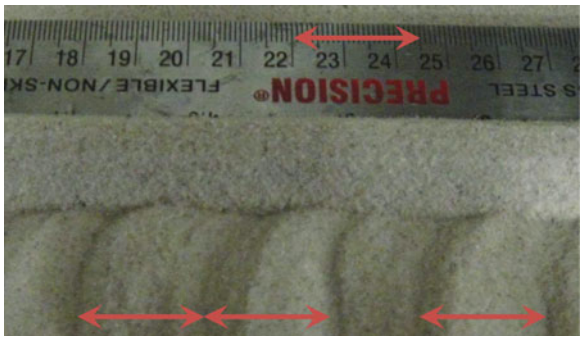

Fig. 2 Example of tread pattern at 75 % slip, 14.9 N normal load

where ϕ is the internal angle of friction, K is the shear deformation modulus, and j can be written in the form used by Ishigami et al. [13]:

$$j(\theta) = r\left[\theta_f - \theta - (1-i)\left(\sin\theta_f - \sin\theta\right)\right] \tag{8}$$

The vertical force F_z, drawbar pull (DP), and torque T are area integrals of the stresses acting on the wheel–soil surface as follows:

$$F_z = rb\int_{\theta_r}^{\theta_f} \left(\tau\left(\theta\right)\sin\theta + \sigma\left(\theta\right)\cos\theta\right) d\theta \tag{9}$$

$$DP = F_x = rb\int_{\theta_r}^{\theta_f} \left(\tau\left(\theta\right)\cos\theta - \sigma\left(\theta\right)\sin\theta\right) d\theta \tag{10}$$

$$T = r^2 b\int_{\theta_r}^{\theta_f} \tau\left(\theta\right) d\theta \tag{11}$$

2.2 Pressure-Sinkage Relationship

The traditional formulation described in the previous section needs to be advanced so that it can account for the oscillations in forces and torques observed by the present authors for a smooth rigid wheel traversing in sandy soil under steady-state slip conditions. Figure 2 shows a sample of the ripples left in the sandy soil behind the wheel for a slip ratio of 0.75 under a 14.9 N normal load, while Fig. 3 plots the corresponding wheel torque and drawbar pull as a function of time, clearly showing the resulting oscillatory pattern. Examining the wheel track in Fig. 2, it can be seen that the distance from valley to valley in the ripples is approximately 23 mm or, correlating this displacement to the travel time, about 1 s. Figure 3 shows that the period of the oscillation is also approximately one second for the torque and drawbar pull measurements.

The steady-state oscillation of the wheel torque suggests that the shear stress $\tau(\theta)$ in Eq. 11 is rising and falling periodically. Presented in Eq. 7, the shear stress is a function of the normal stress $\sigma(\theta)$ and the normal stress is calculated by the pressure–sinkage relationship of Eqs. 1 and 2.

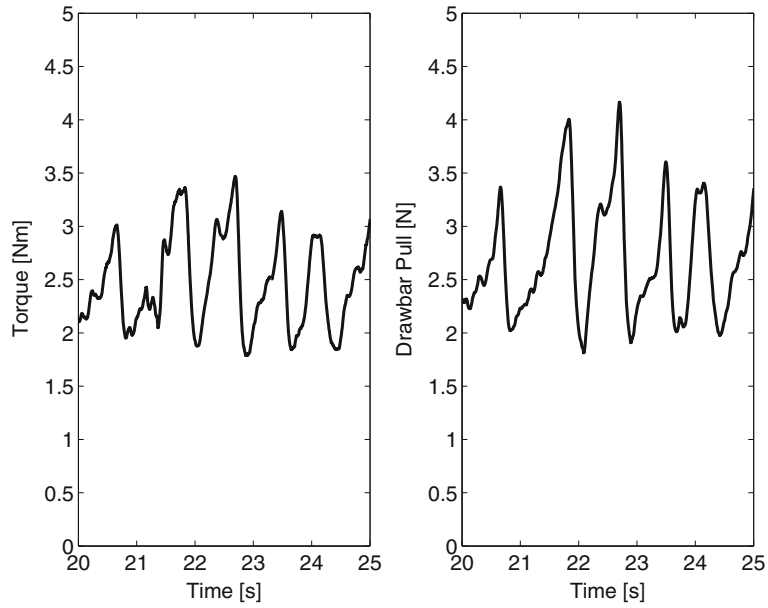

Fig. 3 Example oscillatory pattern in the torque and drawbar pull for a slip ratio of 0.75 and a 14.9 N normal load

Variations and alternative formulations of the pressure–sinkage relationship have been presented [16, 18, 23]. A solution for k in Eq. 1 is given by Bekker [4] as:

$$k = \frac{k_c}{b} + k_\phi \tag{12}$$

so that

$$p = \left(\frac{k_c}{b} + k_\phi\right) z^n \tag{13}$$

where b is the smaller dimension of the contact patch. Wong [23], points out that Eq. 13 is an empirical equation. Moreover, the parameters k_c, k_ϕ are not 'true' soil constants because their values depend on the experimental conditions used to obtain them [6].

Another common pressure–sinkage relationship is the Reece [20] formulation as follows:

$$p = \left(ck'_c + \gamma b k'_\phi\right)\left(\frac{z}{b}\right)^n \tag{14}$$

where the density γ and cohesion c are *true* soil constants. This formulation uses two new dimensionless pressure–sinkage parameters k'_c and k'_ϕ. Reece's model has been verified by using penetration tests at various aspect ratios. The results imply that the pressure p is a function of the terrain's standard material properties: density γ and cohesion c. These parameters are an improvement over the purely empirical parameters obtained from a Bevameter test. One will also notice that Reece's validated relationship of terrain density and pressure dictates that a change in the terrain density will cause a change in the pressure and, as a result, a change in the associated forces and stresses calculated from this pressure–sinkage relationship. Citing Reece's original work [20], Wong [23] suggests that, for dry cohesionless sand, k'_c should be negligible; therefore, k'_c has been set equal to zero for the dry sand testing carried out by the present authors. The authors have left k'_ϕ as a manual tuning parameter for the wheel–soil model proposed in this work.

It is well known that if the density of a substance or terrain increases, the more pressure or force can be exerted on the terrain before it fails. For granular material, such as sand, this phenomenon is especially true [8]. As the void ratio of sand decreases, the strength of the sand increases [8]. The void ratio e is defined as:

$$e = \frac{V_v}{V_s} \tag{15}$$

In general the grain size for the sand used by the present authors is not uniform but has a relatively normal distribution of grain size. Such a grain-size distribution will allow smaller grains to fall into voids created in between the larger grains. When the sand is not fully compacted the void ratio could be high—between 0.65 and 0.85 [8]. If a sample was densely packed, the void ratio could drop to 0.2 or lower. The change in the void ratio directly affects the density and strength of the terrain.

As a wheel travels over and through the sand there are varying degrees of deformation occurring along the soil-wheel interface and within the terrain. There is more deformation at the soil-wheel interface and less deformation as one travels away from the interfacing surfaces. The present authors postulate that the deformation caused by the smooth wheel allows some voids in the terrain to be filled by moving sand particles. This movement will lower the local void ratio, while increasing the local density of the sand around the wheel. This increase in density will cause an increase in the pressure and corresponding normal stress experienced by the wheel which in turn, by virtue of Eqs. 7 and 10, could explain the observed changes in drawbar pull. Wong [22] describes how a terrain reacts with varying pressures for repetitive loading from a tracked vehicle. To help explain the observed oscillations in drawbar pull, this tracked-vehicle theory can also be applied to a wheeled vehicle traversing a generalized sample of material that follows the elastic-plastic-Mohr-Coulomb relationship as illustrated in Fig. 4.

Referring to the left-hand side of Fig. 4, one can see that, as the displacement increases for a given pressure P_1, the stress level will increase to τ_1 (pt B). Now, if the pressure were to increase to P_2, due to a local increase in sand density around the wheel, the stress level would be able to climb to a new level τ_2 (pt C) which was not obtainable by the first confining pressure (because no matter

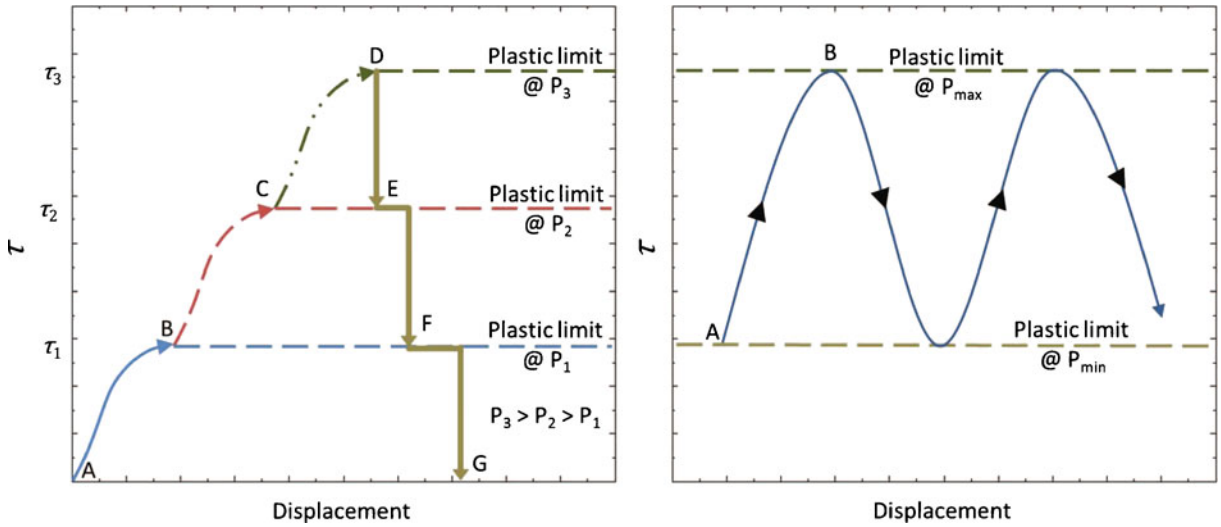

Fig. 4 *Left*: Stress, pressure and displacement relationships [22]; *Right*: Theoretical rise and fall of the shear stress due to the gradual variation in the pressure

how much one displaces the terrain it would continue to plastically deform without an increase in the shear stress). Likewise, if the pressure were to increase further to P_3, the stress would be allowed to climb even higher to τ_3 (pt D). This phenomena could explain the increasing stresses seen in Fig. 3. To account for the decrease in stress one must look at points D–G of Fig. 4. If one was at stress level τ_3 at a confining pressure of P_3 and the pressure were to drop to P_2, as the wheel continues to move forward into fresh (lower-density) sand, or due to an initial shear-stress induced failure and loosening of the soil, the shear-stress would drop to the maximum allowable stress level at P_2 (which would be the plastic limit of the P_2 curve). If the pressure were to drop again to P_1, the stress would drop to the plastic region of the P_1 curve. The continuous displacement of the sand around the wheel would cause the density to gradually increase and the process would repeat. This cyclic loading and unloading due to changes in the local sand density could explain how the shear stress levels are able to fluctuate in the steady-state torque measurements of Fig. 3. The curve in the left-hand side of Fig. 4 has been discretized for the theoretical explanation; however, in reality the change in the confining pressure is not as sudden so that one would not have the exaggerated steps shown in points D–G of Fig. 4. The right-hand side of Fig. 4 shows a more continuous theoretical rise and fall of the shear stress as the pressure gradually varies between $P_{\min}$ and $P_{\max}$. To capture this effect analytically, additional terms need to be added to the traditional wheel–soil model.

2.3 Proposed Model Parameters

From the previous discussion on how local density changes in the terrain around the driven wheel could be responsible for influencing the stresses acting on a smooth rigid wheel while operating in sandy soil (thereby producing the observed oscillations in wheel forces and torque), the present authors propose a new pressure–sinkage relationship as a first approximation to capture this phenomenon:

$$p = \left(ck'_c + \gamma b k'_\phi\right)\left(\frac{z}{b}\right)^n + A_\gamma \sin(\omega t + \Phi) \qquad (16)$$

This formulation uses the Reece pressure–sinkage relationship [20] and adds $A_\gamma \sin(\omega t + \Phi)$ to account for the dynamic changes which oscillate about the mean pressure $p = \left(ck'_c + \gamma b k'_\phi\right)\left(\frac{z}{b}\right)^n$. The $A_\gamma \sin(\omega t + \Phi)$ is a simple sine wave; however, the authors recognize that it could be replaced with a more complex Fourier series. The $A_\gamma \sin(\omega t + \Phi)$ was chosen as a first approximation for the observed phenomena because it is

simple to numerically integrate and allows one to characterize the new A_γ, ω and Φ terms. The higher-order terms in a Fourier series would be difficult to characterize from the current experiments and equipment. Future work could involve exploring these higher-order terms with a modified equipment arrangement specifically designed to characterize the higher-order terms. The resulting new normal stress equation, from Eq. 2, becomes:

$$\sigma(\theta) = \begin{cases} r^n \left(ck'_c + \gamma b k'_\phi\right) \left(\dfrac{\cos\theta - \cos\theta_f}{b}\right)^n \ldots & (\theta_m \leq \theta < \theta_f) \\ \quad + A_\gamma \sin(\omega t + \Phi) & \\ r^n \left(ck'_c + \gamma b k'_\phi\right) \left(\dfrac{\cos\left\{\theta_f - \frac{\theta - \theta_r}{\theta_m - \theta_r}(\theta_f - \theta_m)\right\} - \cos\theta_f}{b}\right)^n \ldots & (\theta_r \leq \theta < \theta_m) \\ \quad + A_\gamma \sin(\omega t + \Phi) & \end{cases} \tag{17}$$

The Φ term in the proposed model is a phase shift that is used to align the model results with experimental data. Based on the discussion of Section 2.2 and the present authors' previous work [11], it is proposed that the amplitude A_γ of the normal stress term in Eq. 17 should be related to the local change in weight density of the soil $d\gamma$ around the wheel, as well as related to the contact length l_c (since this length characterizes the interface between the wheel and the sand that would cause the sand grains to move and fill in the voids). These relationships can be expressed as:

$$A_\gamma \propto l_c d\gamma \tag{18}$$

where l_c is calculated by:

$$l_c = (\theta_f + (-\theta_r))r, \quad \text{or} \quad l_c = \theta_{lc} r \tag{19}$$

One will notice that the proposed relationship in Eq. 18 also satisfies a dimensional analysis. The consistent units occur because the change in weight density has units of [N/m^3], contact length has units of [m], and the result will give amplitude A_γ units of [Pa].

In previous grouser-wheel work [11] the frequency ω in Eq. 16 was directly related to the grouser spacing. The model presented in the current work, however, applies to a smooth rigid wheel (or when the grousers become clogged with terrain) and a different formulation for ω needs to be found. The frequency ω in Eqs. 16 and 17 for a smooth rigid wheel would be expected to be related to the relative motion between the wheel periphery and the terrain. The slip ratio i in Eq. 6 is the quintessential characterization of this relative motion. The proposed resulting relationship is, therefore, as follows:

$$\omega \propto i \tag{20}$$

2.4 Model Implementation

The proposed model was implemented in MATLAB/Simulink. For static and quasi-static analyses in the vertical direction, F_z must equal W; however, the present authors implemented a dynamic model as follows:

$$\sum F = ma \tag{21}$$

$$mg - F_z - F_{\text{damping}} = m_{\text{wheel}} a_z \tag{22}$$

where a_z was solved as part of the numerical simulation. The resulting acceleration was then integrated once for velocity and again to obtain the sinkage. In the simulation mg is held constant while F_z is evaluated via Eq. 9. The damping of the sandy soil F_{damping} was prescribed by viscous damping in the form:

$$F_{\text{damping}} = C_f V_z \tag{23}$$

where V_z is the velocity of the sinkage and C_f is the damping coefficient that was taken as 1300 Ns/m for all normal loads tested. It should be noted that the sinkage predictions obtained from Eq. 22 are dependent on the friction model used. For example, using a viscous friction model in Eq. 22 predicts oscillations in the resulting sinkage for different normal loads applied to the wheel. Corresponding oscillations were also observed in the linear potentiometer measurements of sinkage for all normal loads tested, except for the lowest normal load of 14.9 N. The lack of oscillations measured for this case is attributed to the limited resolution of the potentiometer, combined with non-viscous friction phenomena such as stiction associated with the linear potentiometer and linear bearings which is not captured by a simple viscous friction model (but are more prevalent when normal forces become small enough). For this paper, the authors have chosen to use a viscous friction model in Eq. 22 as it approximated the wheel sinkage to less than 1 % of the wheel diameter.

The computer simulator was designed to emulate the SWTB experiments where the wheel's angular velocity ω_w and forward velocity V_x are prescribed and held constant. The solution methodology for predicting the forces acting on the wheel axle for these experiments is as follows:

1. Input all model constants and constraints
2. Prescribe an initial sinkage value (i.e. 0.001 [m]) for $t = t_o$
3. Determine $\theta_f, \theta_r, \theta_m$
4. Calculate l_c and A_γ from model constants and θ values
5. Compute the stress values $\sigma(\theta)$ and $\tau(\theta)$
6. Compute the drawbar pull F_x and vertical force F_z
7. Use the vertical force F_z and the sum of forces in the vertical direction to calculate the sinkage acceleration
8. Integrate the sinkage acceleration twice to obtain an updated sinkage value and, using this value, return to step 3 for $t = t_o + dt$

Validation of this model was carried out using experimental data collected from a novel SWTB developed at Dalhousie University.

3 Single-Wheel Testbed

Most SWTBs are constructed in the same manner where the sand is placed in a box while the wheel is translated and rotated through the specified terrain [13, 21]. This methodology requires that the wheel translational system be able to accelerate the full wheel assembly, including the wheel support and fixtures, motor, gear train and various sensors, up to the desired speed and then accurately maintain this speed during a test. Given the combined mass of the wheel assembly, this implementation does not easily allow for small normal loads, such as those experienced on Mars or Moon. If a counterbalance was installed to move with the wheel assembly, the resulting design could become more complex, add unwanted dynamic effects, and require larger actuators in the conveyance system when compared to the equivalent SWTB without a counterbalance.

The present authors opted for a different design for the SWTB: translate the terrain while keeping the horizontal wheel assembly motion fixed—with the wheel rotating at a prescribed rotational speed and moving freely in the vertical direction. This novel design was accomplished by converting a Blohm Plamomat 408 computer-numerically-controlled (CNC) creep-feed grinding machine into a SWTB. This grinding machine was ideally suited to be retrofitted as a SWTB given: the extreme rigidity of machine, that its conveyance components are already sealed from abrasives, and that the machine's table is able to support over 700 kg while precisely controlling the 950 mm horizontal movement from 30 to 40,000 mm/min by means of a sophisticated industrial actuation and control system. Moving 700 kg, 950 mm over a wide range of velocities is, in general, not a trivial task but was well within the capabilities of the CNC grinding machine used during this research. One should note that the material properties of a terrain can vary when accelerated too quickly and, therefore, SWTBs that translate the terrain are not well suited for high-speed testing. Throughout the course of this study the terrain never translated faster than 5.6 m/min so that the terrain properties would not vary during a test.

The wheel was allowed to freely move up and down along eight lubricated linear bearings.

Table 1 gives the specifications of the smooth rigid wheel used in this work. The sinkage was recorded by a linear potentiometer. The angular velocity of the wheel was held constant at 0.917 rads/s by a closed-loop control system utilizing tachometer feedback attached to the motor. The forces and moments were recorded by a *JR3* FMS and the torque on the wheel axle was recorded by a FUTEK torque sensor. The FMS was mounted above the motor while the torque sensor was mounted between the wheel and the planetary geartrain. All measurements were acquired via a National Instruments PCI-MIO-16XE-10 board and recorded via a custom LabView program. Since the sensors and drivetrain are only translating in the direction of sinkage, a simple counterbalance was implemented so that relatively small normal loads could be studied analogous to those experienced by rovers on Mars. The wheel was always in contact with the terrain and, therefore, the wheel always experienced a load.

The grinding machine's linear translational control system is extremely accurate with no appreciable vibrations associated with the movement of the grinding machine's table. For the present study, the machine's table speed was varied to control the slip ratio while the wheel's rotational speed was held constant.

The published research involving the MIT SWTB [3, 9, 10] reports that the sand was 15.0 cm deep while Ishigami et al.'s [13] work had 12.0 cm of sand. These sand depths may be suitable for many wheel–soil studies; however, the authors of this work chose to exploit the strength, rigidity and control of the Blohm 408 Plamomat. A sandbox measuring 172.5 cm long by 52.5 cm wide by 29 cm deep was used. The added sand depth allowed the researchers to confidently rule out any wall effects that may influence the studies—especially at higher normal loads and pressures.

Table 1 SWTB parameters

Parameter	Value	Units
Wheel radius r	100	mm
Wheel width b	75	mm
Wheel angular velocity ω_w	0.91	rad/s
Sand depth	290	mm
Horizontal travel	950	mm

4 Experimental Results

This paper hypothesizes that the local density change around a smooth wheel (due to the void ratio changing as the slipping wheel engages the sandy soil) causes the observed oscillations in wheel force and torque measurements. Key to validating this hypothesis is to demonstrate that the void ratio of the sand can alter quickly when excited.

Figure 5 shows time-lapse images of the experimental sand on a shaker table which is producing a 30Hz sinusoidal excitation with a displacement of 2 mm. In the figure the entire sandbox is moving in the horizontal direction (left to right). It can be seen that within 0.5 s there is over a 6.5 % change in the volume (or density) and within 3 s there is a 14 % change in volume; therefore, the experimental sand's density is sensitive to small amounts of displacement lending credibility to the current authors' hypothesis.

This result also highlights the importance of ensuring that, after each experimental test with the SWTB, the sand be thoroughly mixed before being leveled to ensure that an initial loose randomly-packed soil structure and void ratio of the terrain is maintained to ensure repeatability of the experimental results.

Tests were performed by adding mass to the SWTB resulting in three different normal load conditions (14.9 N, 47.7 N and 63.9 N) for the smooth wheel described in Table 1. The normal load conditions refer to the *weight* of the system. The benchmark for the model development was the 14.9 N normal load case and experiments were carried out with this loading condition for slip ratios of 0.25, 0.50, 0.60, 0.75 and 0.90. The other two normal loads (47.7 N and 63.9 N) were used for model validation, and experiments were carried out for slip ratios of 0.25, 0.50, 0.75 and 0.95. In each loading case, once the drawbar pull was positive, ripples were noticed in the track of the wheel and corresponding oscillations were observed in the experimental data. When examining the wheel torque data it was discovered that the amplitude of the oscillations grew as the slip ratio and normal load increased. These results can be seen in Fig. 6 (left). The data marks on the graph show the mean oscillatory amplitude values of the torque while

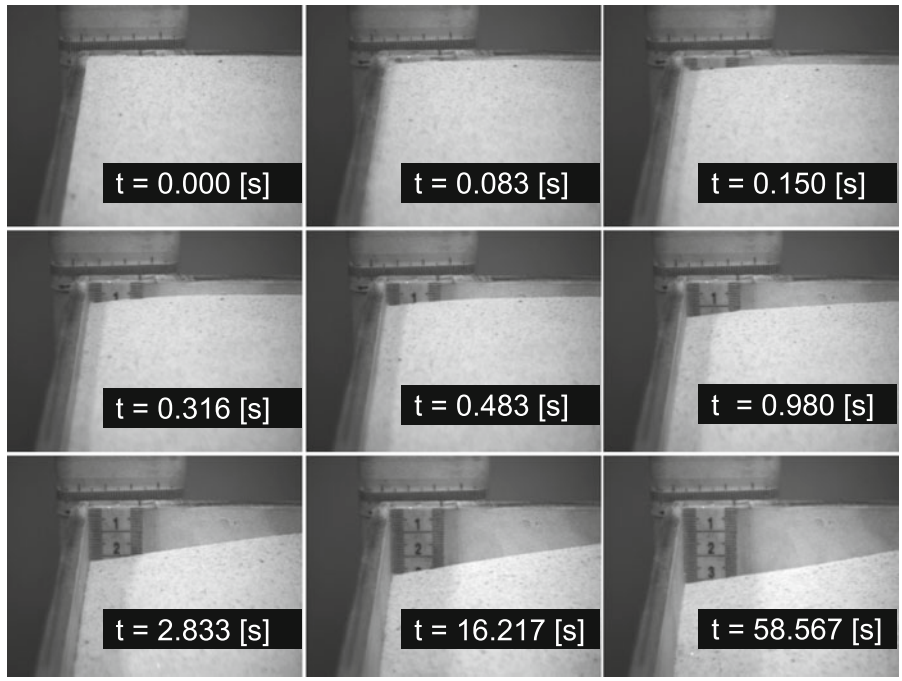

Fig. 5 Shaking sand

the bounding bars indicate the torque oscillation limits for each scenario.

It was found that the oscillatory mean amplitude trend seen in Fig. 6 (left) for the three different test cases followed a similar trend as that observed for sinkage as seen in Fig. 6 (right). The contact length l_c is directly related to the sinkage and is also a function of the normal load. Moreover, l_c is the characteristic length which represents the wheel–soil interface that would cause the sand grains to fill in the voids of the terrain structure. Figure 7 plots the amplitude of the torque oscillations as a function of the contact length revealing a linear relationship. Furthermore, the slope of the fitted line for each normal load condition is similar. The R^2 value for the 14.9 N, 47.7 N and 63.9 N normal loads are 0.91, 0.90 and 0.85, respectfully.

Therefore, this smooth-wheel model development confirms that A_γ from Eq. 18 is indeed a

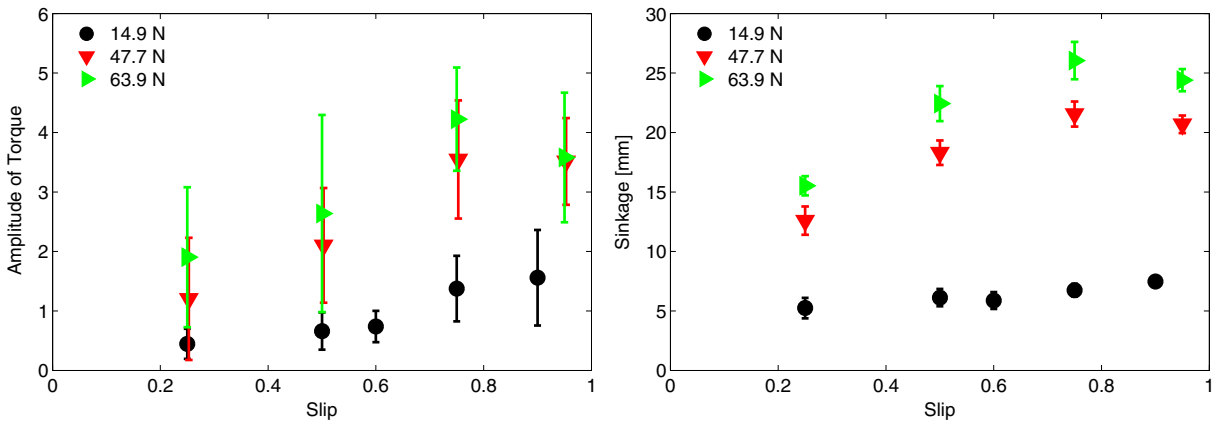

Fig. 6 *Left*: Amplitude of torque oscillations. *Right*: Sinkage data

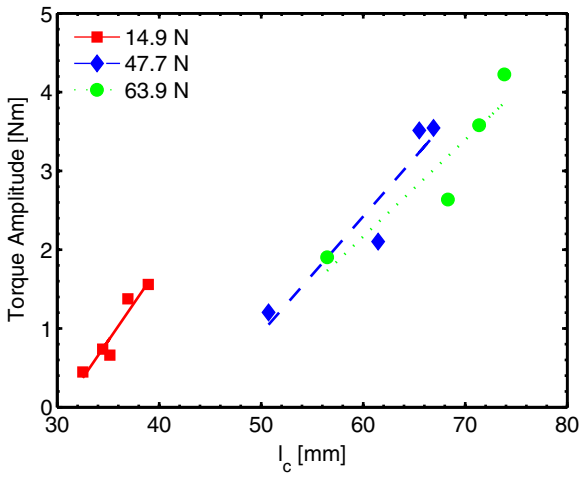

Fig. 7 Amplitude of torque oscillations vs. the contact length

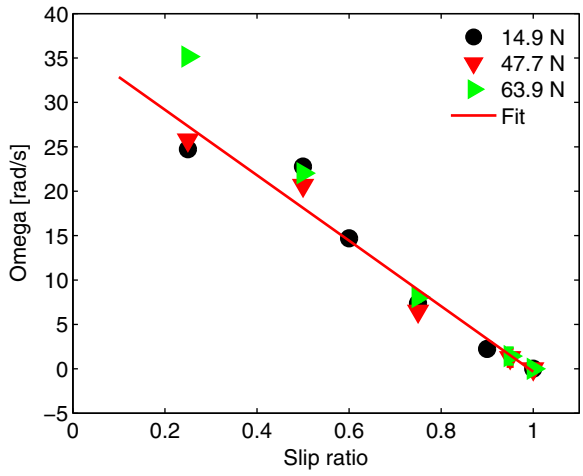

Fig. 8 Omega vs slip ratio curve fitting

linear function of the contact length and can be written as:

$$A_\gamma = l_c \cdot d\gamma \cdot k'_a \tag{24}$$

where k'_a is a dimensionless amplitude factor which was tuned to 110 for all test cases in the current study.

The results from this analysis introduce one non-dimensional scaling factor k'_a, which the present authors term the *Amplitude Factor*. If a terrain does not exhibit the observed oscillations, k'_a would be zero and the result would be the traditional wheel–soil model. It should also be mentioned that if there is no change in the terrain's density there would be no oscillations in the simulated data as the additional term in the new pressure–sinkage equation would be zero. For the simulations performed in this study a value of $\gamma \cdot 0.10$ was used for $d\gamma$. This value implies that the density varied by 10 % from the nominal value γ. The 10 % variation change in density appeared reasonable for a slipping wheel given the 6.5 % change (0.5 s) and 14 % change (3.0 s) observed in Fig. 5.

While the present authors' previous grouser-wheel work [11] related the number of grousers to the frequency parameters ω, a new formulation for this term is needed for the case of a smooth wheel. The frequency of the oscillations was plotted against the slip ratio and the 14.9 N benchmark normal load was used to develop a relationship between ω and i. The other two normal loads of 47.7 N and 63.9 N were again used as test cases to validate the model. Figure 8 shows the relationship between the frequency of the oscillations and slip ratio for all normal loads examined. A first order least-squares fit was performed on the 14.9 N normal load data, as proposed by Eq. 20 in Section 2.3, resulting in:

$$\omega = -36.9i + 36.5 \tag{25}$$

With a goodness-of-fit (R^2) value of 0.94, Eq. 25 reasonably approximates the frequency of the oscillations for all normal loads and slip ratios studied.

The proposed wheel–soil model parameters were calibrated with the benchmark normal load

Table 2 Model parameters

Parameter	Value	Units	Comments
c	0.0	kPa	Soil cohesion
ϕ	28	deg	Internal angle of friction
k'_ϕ	900		Pressure–sinkage modulus
k'_c	0		Pressure–sinkage modulus
k'_a	110		Pressure–sinkage modulus
η	0.5 or 0.95		Sinkage coefficient
γ	13734	kg/m^{2}s^2	Soil weight density
a_0	0.4		Used to determine θ_m
a_1	0.2		Used to determine θ_m
F_{damping}	1300	Ns/m	Vertical viscous friction

of 14.9 N and then the performance of the model was validated using the 47.7 N and 63.9 N loading conditions. Table 2 summarizes the model parameters used.

The only model parameter that varied from one simulation to another is η which was determined from observed measurements during testing on the SWTB. For the 14.9 N normal load, η was visually inspected to be 0.85 in all of the slip ratio cases examined at this normal load. For the 47.7 N normal load, η was again visually inspected to be 0.5 for the 0.25, 0.50 and 0.75 slip ratio cases, and 0.85 for the 0.95 slip ratio case. Finally, for the 64.9 N normal load, η was approximated at 0.6 for all of the slip ratio cases studied.

To obtain a mean value for each test case, the experimental data was averaged over five test runs during a steady-state operating period. Based on the slip ratio employed, the length of this steady-state operating period varied. This variable length occurs because the linear velocity of the terrain is altered to control the slip ratio and, as a result, the duration which it takes to travel 950 mm varies for each slip ratio. For example, a 0.25 slip experiment lasts a total of 13 s with a steady-state region of 2–7 s, which is in contrast to a 0.95 slip run which takes 207 s to complete, with over 200 s of steady-state operation. A sample rate of 1000 Hz was used for all tests.

It is important to note that the model was examined over a wide range of slip conditions which a lightweight vehicle could encounter. Slip ratios of 0.75 and 0.95 are neither desirable nor ideal; however, they may be unavoidable. For example, NASA's Mars Exploration Rover, "Spirit", was entrenched for several weeks and would often operate in high-slip conditions [2]. As extra-terrestrial exploration continues, rovers will continue to find themselves in high-slip conditions and, therefore, there is a need to better model these operation conditions for designers and mission specialists.

There are various models [4, 13, 18, 23] which are specifically designed to predict the mean values of the wheel–soil interaction. The present work does not focus on the mean values of the wheel–soil interaction but rather the deviations and oscillations about the means. Thus, to highlight the current work's contributions to the field, a series of mean-adjusted overlays of the predicted and experimental drawbar pull are displayed in Fig. 9 for a representative number of test cases. In these graphs, the mean of both the experimental and simulation data has been shifted to zero so that the amplitude and phase of the new model terms can be easily examined and compared. The experimental data shown in Fig. 9 are for a representative single experiment since averaging the data over several repeatability experiments would distort the amplitude and phase of the oscillations. When the means of the vertical forces were compared for all tests, the average error was 1.96 N with a standard deviation of 0.9.

Figure 9a overlays the experimental data and the simulation data for 5 s with a 14.9 N normal load and a slip ratio of 0.25. It can be seen that, on this relatively long time scale, the model is able to generally reproduce the amplitude of the oscillations. One will notice slight irregularities and disturbances in the experimental oscillations at about 1.9 s which is attributed to the sand's natural and inherent local variability in the void ratio; hence, the density of the terrain is also variable prior to the wheel–soil interaction. It is unrealistic and unfeasible to have a perfectly-uniform void ratio in the sand prior to a test. As a consequence, if the terrain has a section with slightly more or slightly fewer voids in a specific area, the result would be that the frequency and amplitude of the oscillations of the wheel–soil interaction will vary due to the sand's pre-existing state. However, on average, the equations presented in Section 2.2 capture the overall phenomena. One could add stochastic variables to the model if these delays or variations are of importance. Adding higher-order terms to the dynamic model could also assist in modelling these variations; however, characterizing the additional terms would not be trivial and the added resulting terms may not be related to known physical soil constants. The current state of the proposed model is a significant improvement over previous traditional analytical models as these traditional models do not capture any of the oscillatory amplitude or frequency variations.

Figure 9b overlays the experimental data and the simulation data for 10 s with a 14.9 N normal load and a slip ratio of 0.5. The model is again able to capture the amplitude and frequency

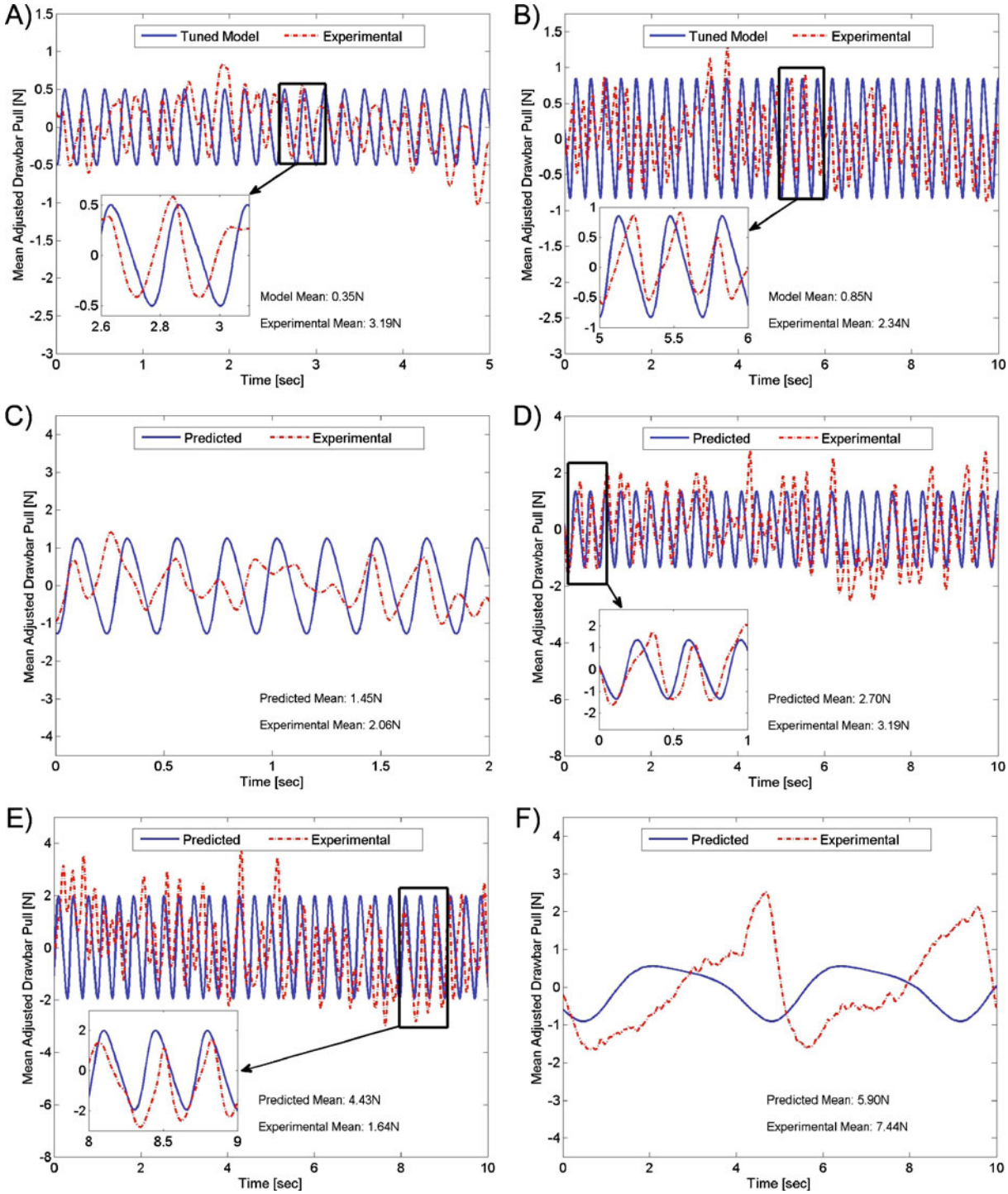

Fig. 9 Comparison between experimental work and model. **a** 14.9 N normal load, 0.25 slip; **b** 14.9 N normal load, 0.50 slip; **c** 47.9 N normal load, 0.25 slip; **d** 47.9 N normal load, 0.50 slip; **e** 63.9 N normal load, 0.50 slip; **f** 47.9 N normal load, 0.95 slip

characteristics of the oscillations. These results are typical for slip conditions at the 14.9 N normal load.

As mentioned earlier, the model was tuned using the 14.9 N normal load, while the other two normal loads of 47.7 N and 63.9 N were used as test cases to examine the model's predictive capabilities.

Figure 9c overlays the experimental data and the simulation data for 2 s with a 47.9 N normal load and a slip ratio of 0.25. For this case the model is also able to effectively predict the amplitude and generally approximate the frequency of the oscillations. Again one will notice slight disturbances in the experimental oscillations due to natural variations in the local sand density that the model currently does not account for.

Figure 9d shows the experimental data and the simulation data for 10 s with a 47.9 N normal load and a slip ratio of 0.50. These results are representative of most cases at the 47.9 N normal load.

Figure 9e overlays the experimental data and the simulation data and highlights the ability to predict both the amplitude and frequency of the oscillations at the highest normal load in the study (63.9 N). These results are also representative of most cases at the 63.9 N normal load.

The highest slip ratio case of 0.95 revealed the upper limit of the model's prediction capabilities. Figure 9f shows that the model is able to predict the frequency of the oscillations; however, the amplitude is under predicted at a slip ratio of 0.95 with a normal load of 47.9 N. This under prediction was also found in the 63.9 N normal load at the 0.95 slip ratio. Note that the dimensionless *Amplitude Factor* could be tuned to better represent the experimental data if more accuracy at a slip ratio of 0.95 is desired.

5 Conclusions

This work presents a new dynamic pressure–sinkage relationship for modeling the observed oscillations in drawbar pull for a smooth rigid wheel on dry sand. The proposed model was validated over a wide range of slip ratios and normal loads. The SWTB used for the validation is unique since the terrain is translated instead of the wheel assembly. Also, the SWTB is capable of very small normal loads because of the counterbalance system employed.

The experimental data showed a repeatable low-frequency oscillation in the force data that could be correlated to visual ripples in the track left by the smooth rigid wheel. The proposed model accounts for this harmonic by adding an $A\sin(\omega t+\phi)$ term into the traditional pressure–sinkage relationship. The final form of the new dynamic pressure–sinkage relationship for a smooth wheel is:

$$p=\left(ck_c'+\gamma b k_\phi'\right)\left(\frac{z}{b}\right)^n+d\gamma l_c k_a'\sin(\omega t+\phi) \tag{26}$$

The experimental results show an improvement over existing smooth-wheel models (which fail to capture any oscillations about the predicted means). The new model provides a fundamental basis to increase the fidelity of wheel–soil models for lightweight mobile robots. Previous grouser-wheel work [11] is not applicable because, for a smooth wheel, the frequency of the oscillations is a function of the slip ratio rather than the number of grousers. In addition, for the case of a wheel with grousers, the spaces between the grousers may become filled with compacted terrain such that the wheel behaves like a smooth wheel and the added tractive benefit of the grousers is severely diminished. Remotely operated vehicles are particularly vulnerable to this wheel clogging phenomenon as there may not be an opportunity to clean the wheels once they become filled with terrain. It is in these situations where the proposed smooth wheel model derived in the present work should also be used to better predict the tractive effort of the wheels and vehicle behaviour. Furthermore, in the case of a scarcely-lugged/grouser wheel, Eq. 26 can be used to model the wheel–soil interaction between the lugs to help achieve a closer approximation to the drawbar pull. The increased fidelity and predictive qualities of the new model can also aid in future wheel designs as well as in assessing mobility capabilities of various mobile robots. Future work with this model could be carried out to examine the higher-order

frequencies that appear in the experimental data which are not modelled in this work.

Acknowledgements The authors would like to thank the Natural Sciences and Engineering Research Council of Canada (NSERC) and the Canadian Foundation for Innovation (CFI) for their financial support of this research. The authors would also like to thank Shaw Brick for donating the test sand.

References

1. Apostolopoulos, D., Wagner, M., Heys, S., Teza, J.: Results of the inflatable robotic rover testbed. Tech. Rep. CMU-RI-TR-03-18, Carnegie Mellon University (2003)
2. Arvidson, R., Bell III, J., Bellutta, P., Cabrol, N., Catalano, J., Cohen, J., Crumpler, L., Des Marais, D., Estlin, T., Farrand, W., et al.: Spirit Mars Rover Mission: overview and selected results from the northern Home Plate Winter Haven to the side of Scamander crater. J. Geophys. Res **115**, 1–19 (2010)
3. Bauer, R., Leung, W., Barfoot, T.: Experimental and simulation results of wheel–soil interaction for planetary rovers. In: 2005 IEEE/RSJ International Conference on Intelligent Robots and Systems (IROS 2005), pp. 586–591. IEEE (2005)
4. Bekker, M.: Introduction to Terrain-Vehicle Systems. University of Michigan Press, Ann Arbor (1969)
5. Fervers, C.: Improved fem simulation model for tire-soil interaction. J. Terramechs. **41**(2–3), 87–100 (2004)
6. Hambleton, J., Drescher, A.: Development of improved test rolling methods for roadway embankment construction. Final Report MN/RC 2008-08, University of Minnesota. Dept. of Civil Engineering (2008)
7. Hegedus, E.: A simplified method for the determination of bulldozing resistance. Land Locomotion Research Laboratory, Army Tank Automotive Command Report, 61 (1960)
8. Holtz, R., Kovacs, W.: An Introduction to Geotechnical Engineering, vol. 733. Prentice-Hall (1981)
9. Iagnemma, K., Kang, S., Shibly, H., Dubowsky, S.: Online terrain parameter estimation for wheeled mobile robots with application to planetary rovers. IEEE Trans. Robot. **20**(5), 921–927 (2004)
10. Iagnemma, K., Shibly, H., Dubowsky, S.: On-line terrain parameter estimation for planetary rovers. In: IEEE International Conference on Robotics and Automation (ICRA'02), vol. 3, pp. 3142–3147. IEEE (2002)
11. Irani, R., Bauer, R., Warkentin, A.: A dynamic terramechanic model for small lightweight vehicles with rigid wheels and grousers operating in sandy soil. J. Terramechs. **48**(4), 307–318 (2011)
12. Ishigami, G.: Terramechanics-based analysis and control for lunar/planetary exploration robots. Phd, Tohoku University, Department of Aerospace Engineering (2008)
13. Ishigami, G., Miwa, A., Nagatani, K., Yoshida, K.: Terramechanics-based model for steering maneuver of planetary exploration rovers on loose soil. J. Field Robot. **24**(3), 233–250 (2007)
14. Janosi, Z., Hanamoto, B.: The analytical determination of drawbar pull as a function of slip for tracked vehicle in deformable soils. In: 1st Int. Conf. on Terrain-Vehicle Systems. Torino, Italy (1961)
15. Khot, L., Salokhe, V., Jayasuriya, H., Nakashima, H.: Experimental validation of distinct element simulation for dynamic wheel–soil interaction. J. Terramechs. **44**(6), 429–437 (2007)
16. Lyasko, M.: LSA model for sinkage predictions. J. Terramechs. **47**(1), 1–19 (2010)
17. Maciejewski, J., Jarzbowski, A.: Experimental analysis of soil deformation below a rolling rigid cylinder. J. Terramechs. **41**(4), 223–241 (2004)
18. Meirion-Griffith, G., Spenko, M.: A modified pressure–sinkage model for small, rigid wheels on deformable terrains. J. Terramechs. **48**(2), 149–155 (2011)
19. Nakashima, H., Fujii, H., Oida, A., Momozu, M., Kawase, Y., Kanamori, H., Aoki, S., Yokoyama, T.: Parametric analysis of lugged wheel performance for a lunar microrover by means of DEM. J. Terramechs. **44**(2), 153–162 (2007)
20. Reece, A.: Principles of soil–vehicle mechanics. Proc. Inst. Mech. Eng. **180**(1965), 45–66 (1965)
21. Shibly, H., Iagnemma, K., Dubowsky, S.: An equivalent soil mechanics formulation for rigid wheels in deformable terrain, with application to planetary exploration rovers. J. Terramechs. **42**(1), 1–13 (2005)
22. Wong, J.: Terramechanics and Off-road Vehicles. Elsevier (1989)
23. Wong, J.: Theory of Ground Vehicles. Wiley, New York (2001)
24. Wong, J., Reece, A.: Prediction of rigid wheel performance based on the analysis of soil–wheel stresses part I. Performance of driven rigid wheels. J. Terramechs. **4**(1), 81–98 (1967)